COBEM 2021 26th International Congress of Mechanical Engineering
November 22-26, 2021, Virtual Congress, Brazil
ABCM Associação Brasileira de Engenharia e Ciências Mecânicas

COB-2021-0388
A COMPARISON OF LOW AND HIGH-ORDER METHODS FOR THE SIMULATION OF SUPERSONIC JET FLOWS

Diego F. Abreu
Instituto Tecnológico de Aeronáutica, 12228–900, São José dos Campos, SP, Brazil
mecabreu@yahoo.com.br

Carlos Junqueira-Junior
Arts et Métiers Institute of Technology, DynFluid, CNAM, HESAM University, 151 Boulevard de l'Hôpital, 75013, Paris, France
junior.junqueira@ensam.eu

Eron T. V. Dauricio
Instituto Tecnológico de Aeronáutica, 12228–900, São José dos Campos, SP, Brazil
eron.tiago90@gmail.com

João Luiz F. Azevedo
Instituto de Aeronáutica e Espaço, 12228–904, São José dos Campos, SP, Brazil
joaoluiz.azevedo@gmail.com

Abstract. *The present work compares results for different numerical methods in search of alternatives to improve the quality of large-eddy simulations for the problem of a supersonic turbulent jet flows. Previous work has analyzed supersonic jet flows using a second-order, finite difference solver based on structured meshes, and the results indicated a shorter potential core of the jet and different levels of velocity fluctuations. In the present work, the results of previous simulations are compared to new results using a high-order, discontinuous Galerkin solver for unstructured meshes. All simulations are performed keeping the total number of degrees of freedom constant. The results of the current simulations present very similar mean velocity distributions and slightly smaller velocity fluctuations, and they seem to correlate better with the experimental data. The present results indicate that additional studies should focus on the jet inlet boundary conditions in order to improve the physical representation of the early stages of the jet development.*

Keywords: *Jet flows, Large Eddy Simulation, Discontinuous Galerkin Method*

1. INTRODUCTION

The use of large-eddy simulations (LES) for solving compressible turbulent jets is growing due to the ability to provide sufficiently good solutions at a reasonable cost, when compared to direct numerical simulations (DNS) or the realization of physical experiments. The application of LES on jet flows is interested in obtaining the flow and temperature fields, providing information for aerodynamics, acoustics and heat transfer analyses.

There are many numerical options to perform LES for compressible turbulent flows. Two major distinct approaches are based on low-order methods and high-order methods. When using low-order methods, the good results are obtained from sufficiently fine grids or using adaptive mesh algorithms. The group of high-order methods, instead of depending on fine grids, chooses to work with more sophisticated numerical algorithms for solving the physical equations that allow a more rigorous representation of the equations calculated. Moreover, since high-order methods implicitly increase the number of degrees of freedom, it is possible to have less refined meshes when compared to the low-order methods.

A compressible LES tool, JAZzY, was specifically designed to generate unsteady flow data of compressible turbulent jets based on a second-order spatially accurate method for structured grids. A validation of JAZzY is performed in Junqueira-Junior *et al.* (2018) for a supersonic jet flow configuration. The validation results indicate a shorter potential core of the jet when compared to experimental and numerical data. The potential core of the jet is defined as the position in the centerline of the jet where the velocity equals 95% of the jet velocity. Moreover, one can also observe a mismatch of the mean velocity profiles along the lipline when comparing to the references. The shorter potential core is achieved when using JAZzY with different mesh refinements and subgrid-scale (SGS) models.

Structured, low-order methods require very refined meshes near the core of the jet and such an approach does not allow local mesh refinement. Therefore, the cost of calculations is prohibitive. Once the strategy of using structured grids showed some disadvantages for the problem of interest, the authors decided to investigate the possibilities using

an unstructured, high-order framework, FLEXI (Krais *et al.*, 2021), which implements the discontinuous Galerkin (DG) method proposed by Kopriva and Gassner (2010) and Hindenlang *et al.* (2012). The FLEXI tool applies a discretization that can be employed on unstructured meshes, thus providing more flexibility with regard to geometries and meshes. The order of accuracy of the numerical algorithm varies by choosing different polynomial degrees for interpolating the solution inside each element. The numerical code is open-source and it is already validated with interesting results at reasonable costs (Gassner and Beck, 2013).

The present work is interested in comparing the effects of the DG method and the structured 2nd-order spatial discretization approach on the solution of supersonic jet flows. The comparisons presented here investigate the quality of the results from low-order simulations with the two methodologies and the results using FLEXI with third-order accuracy. The results are also compared with experimental data. One important aspect of the present study is the comparison of different approaches when using similar meshes topologies with, also, similar numbers of degrees of freedom in the simulations and, hence, comparable computations resources.

2. NUMERICAL FORMULATION

2.1 Governing Equations

The governing equations to be solved by both numerical methods are the compressible filtered Navier-Stokes equation. In conservative form, they can be expressed by

$$\frac{\partial \bar{\mathbf{Q}}}{\partial t} + \nabla \cdot \mathbf{F}(\bar{\mathbf{Q}}, \nabla \bar{\mathbf{Q}}) = 0, \tag{1}$$

where $\bar{\mathbf{Q}} = [\bar{\rho}, \bar{\rho}\tilde{u}, \bar{\rho}\tilde{v}, \bar{\rho}\tilde{w}, \bar{\rho}\check{E}]^T$ is the vector of filtered conserved variables and $\mathbf{F}$ is the flux vector. The flux vector can be divided into the Euler fluxes and the viscous flux, $\mathbf{F} = \mathbf{F}^e - \mathbf{F}^v$. The fluxes with the filtered variables may be written as

$$\mathbf{F}_i^e = \begin{bmatrix} \bar{\rho}\tilde{u}_i \\ \bar{\rho}\tilde{u}\tilde{u}_i + \delta_{1i}\bar{p} \\ \bar{\rho}\tilde{v}\tilde{u}_i + \delta_{2i}\bar{p} \\ \bar{\rho}\tilde{w}\tilde{u}_i + \delta_{3i}\bar{p} \\ (\bar{\rho}\check{E} + \bar{p})\tilde{u}_i \end{bmatrix} \qquad \mathbf{F}_i^v = \begin{bmatrix} 0 \\ \tau_{1i}^{mod} \\ \tau_{2i}^{mod} \\ \tau_{3i}^{mod} \\ \tilde{u}_j\tau_{ij}^{mod} - q_i^{mod} \end{bmatrix} \qquad \text{, for } i = 1, 2, 3, \tag{2}$$

where $\tilde{u}_i$ or $(\tilde{u}, \tilde{v}, \tilde{w})$ are the Favre averaged velocity components, $\bar{\rho}$ is the filtered density, $\bar{p}$ is the filtered pressure and $\bar{\rho}\check{E}$ is the filtered total energy per unit volume. The terms τ_{ij}^{mod} and q_i^{mod} are the modified viscous stress tensor and heat flux vector, respectively, and δ_{ij} is the Kronecker delta. The filtered total energy per unit volume, according to the definition proposed by Vreman (1995) in its "system I", is given by

$$\bar{\rho}\check{E} = \frac{\bar{p}}{\gamma - 1} + \frac{1}{2}\bar{\rho}\tilde{u}_i\tilde{u}_i. \tag{3}$$

The filtered pressure, Favre averaged temperature and filtered density are correlated using the ideal gas equation of state $\bar{p} = \bar{\rho}R\tilde{T}$, and R is the gas constant, written as $R = c_p - c_v$. The properties c_p and c_v are the specific heat at constant pressure and volume, respectively. The modified viscous stress tensor may be written as

$$\tau_{ij}^{mod} = (\mu + \mu_{SGS})\left(\frac{\partial \tilde{u}_i}{\partial x_j} + \frac{\partial \tilde{u}_j}{\partial x_i}\right) - \frac{2}{3}(\mu + \mu_{SGS})\left(\frac{\partial \tilde{u}_k}{\partial x_k}\right)\delta_{ij} \tag{4}$$

where μ is the dynamic viscosity coefficient, calculated by Sutherland's Law, and μ_{SGS} is the SGS dynamic viscosity coefficient, which is provided by the subgrid-scale model. The strategy of modeling the subgrid-scale contribution as an additional dynamic viscosity coefficient is based on the Boussinesq hyphotesis. The modified heat flux vector, using the same modeling strategy, is given by

$$q_i^{mod} = -(k + k_{SGS})\frac{\partial \tilde{T}}{\partial x_i} \tag{5}$$

where k is the thermal conductivity coefficient of the fluid and k_{SGS} is the SGS thermal conductivity coefficient given by

$$k_{SGS} = \frac{\mu_{SGS}c_p}{Pr_{SGS}} \tag{6}$$

and Pr_{SGS} is the SGS Prandtl number. The work of Junqueira-Junior *et al.* (2018) compares the effects of different SGS models on the simulations of jet flows, and it observes a weak influence of the models. Therefore, the present work only applies the static Smagorinsky model (Smagorinsky, 1964) in order to calculate the subgrid-scale contribution.

2.2 Nodal Discontinuous Galerkin Method

The nodal Discontinuous Galerkin method used in this work is obtained initially by dividing the physical domain Ω into multiple non-overlapping elements. Galerkin methods are capable of handling any element type, however, it is decided to restrict the shape of the elements to hexahedra. When working with hexahedral elements, the implementations is simpler and the computational efficiency is improved when compared to arbitrary shape elements.

The elements from the physical domain are mapped onto a reference unit cube elements $E = [-1, 1]^3$. The equations, presented in (1) need also to be mapped to this new reference domain, leading to

$$J\frac{\partial \bar{\mathbf{Q}}}{\partial t} + \nabla_\xi \cdot \bar{\mathcal{F}} = 0, \tag{7}$$

where ∇_ξ is the divergence operator with respect to the reference element coordinates, $\xi = (\xi^1, \xi^2, \xi^3)^T$, $J = |\partial \mathbf{x}/\partial \xi|$ is the Jacobian of the coordinate transformation and $\bar{\mathcal{F}}$ is the contravariant flux vector.

The discontinuous Galerkin formulation is obtained multiplying (7) by the testfunction $\psi = \psi(\xi)$ and integrating over the reference element E

$$\int_E J\frac{\partial \bar{\mathbf{Q}}}{\partial t}\psi d\xi + \int_E \nabla_\xi \cdot \bar{\mathcal{F}}\psi d\xi = 0. \tag{8}$$

It is possible to obtain the weak form of the scheme by integrating by parts the second term in (8)

$$\frac{\partial}{\partial t}\int_E J\bar{\mathbf{Q}}\psi d\xi + \int_{\partial E} (\bar{\mathcal{F}} \cdot \vec{N})^* \psi dS - \int_E \bar{\mathcal{F}} \cdot (\nabla_\xi \psi) d\xi = 0, \tag{9}$$

where $\vec{N}$ is the unit normal vector of the reference element faces. Because the discontinuous Galerkin scheme allows discontinuities in the interfaces, the surface integral above is ill-defined. In this case, a numerical flux, $\bar{\mathcal{F}}^*$, is defined, and a Riemann solver is used to compute the value of this flux based on the discontinuous solutions given by the elements sharing the interface.

For the nodal form of the discontinuous Galerkin formulation, the solution in each element is approximated by a polynomial interpolation of the form

$$\bar{\mathbf{Q}}(\xi) \approx \sum_{p,q,r=0}^{N} \bar{\mathbf{Q}}_h(\xi_p^1, \xi_q^2, \xi_r^3, t)\phi_{pqr}(\xi), \tag{10}$$

where $\bar{\mathbf{Q}}_h(\xi_p^1, \xi_q^2, \xi_r^3, t)$ is the value of the vector of conserved variables at each interpolation node in the reference element and $\phi_{pqr}(\xi)$ is the interpolating polynomial. For hexahedral elements, the interpolating polynomial is a tensor product basis with degree N in each space direction

$$\phi_{pqr}(\xi) = l_p(\xi^1) l_q(\xi^2) l_r(\xi^3), \quad l_p(\xi^1) = \prod_{\substack{i=0 \\ i\neq p}}^{N_p} \frac{\xi^1 - \xi_i^1}{\xi_p^1 - \xi_i^1}. \tag{11}$$

The definitions presented are applicable to other two directions.

The numerical scheme used in the simulations have a split formulation, as presented by Pirozzoli (2011), with the discrete form given by Gassner *et al.* (2016), to enhance the stability of the simulation. The split formulation is employed to Euler fluxes only. The solution and the fluxes are interpolated and integrated at the nodes of a Gauss-Lobatto Legende quadrature, which presents the summation-by parts property, that is necessary to employ the split formulation.

The Riemann solver used in the simulations is a Roe scheme with entropy fix (Harten and Hyman, 1983) to ensure that second law of thermodynamics is respected, even with the split formulation. For the viscous flux, since the discontinuous Galerkin scheme are not suitable for discretizing the high order derivative operator, the lifting scheme of Bassi and Rebay (1997) is used. The time marching method chosen is the five-stage, fourth-order explicit Runge-Kutta scheme of Carpenter and Kennedy (1994). The shock waves that appear in the simulation are stabilized by using the sub-cell shock capturing method of Sonntag and Munz (2017).

2.3 Second-Order Finite Difference Method

The code JAZzY (Junqueira-Junior *et al.*, 2018) solves the non-dimensional filtered Navier-Stokes equations using a structured finite difference approach for a general curvilinear coordinate system. It calculates the numerical fluxes using a second-order centered scheme with explicit addition of artificial dissipation, which is obtained from the anisotropic scalar model of Turkel and Vatsa (1994). The time integration is done by an explicit second-order five-stage Runge-Kutta scheme (Jameson and Mavriplis, 1986). Even though the simulation is performed for a supersonic problem, no additional shock-capturing model is required, because the Turkel and Vatsa (1994) artificial dissipation model can provide additional artificial dissipation near discontinuities

3. EXPERIMENTAL CONFIGURATION

Most of recent jet experiments are concerned with representing the sound emitted from modern airplanes in takeoff configuration, in which the jet flow is in high subsonic regime. However, our focus is to represent supersonic jet flows, that can be found in large launch vehicles. The experimental work of (Bridges and Wernet, 2008) provided the physics characteristics desired for the simulation in which a group of nozzle configurations is analyzed to obtain different types of jet flows.

The present work studies the fully expanded free jet flow configuration with a Mach number of 1.4. This choice is motivated by the lack of wall geometries and the absence of strong shock waves in the configuration. Such flow characteristics can contribute to reducing the calculation costs. The experimental apparatus for this configuration is composed of a convergent-divergent nozzle designed with the method of characteristics to obtain this flow configuration (Bridges and Wernet, 2008). The nozzle exit diameter is 50.8 mm. The Reynolds number based on the nozzle exit diameter reaches values of approximately 1.65×10^6, which is large compared to most other jet experiments and LES available in the literature.

The data acquisition in the tests applies Time-Resolved Particle Image Velocimetry (TRPIV), and it is operated primarily with a 10 kHz sample rate. For spectra analysis, in some smaller fields, the acquisition is made with 25 kHz. The experiment uses two sets of cameras, one positioned to better capturing the flow along the nozzle centerline and the other to capture the flow of the mixing layer along the nozzle lipline.

4. NUMERICAL SETUP

4.1 Geometry Characteristics

In the present work, the authors decided to utilize the geometry that provided the best results in the work of Junqueira-Junior *et al.* (2018). Such a configuration has a divergent shape with an axis length of $40D$. Close to the jet inlet, one can find a smaller diameter of $16D$ and, on the opposite side, it presents a diameter of $25D$. The code JAZzY is non-dimensional and the reference length is the exit nozzle diameter D. The simulations using FLEXI are dimensional. Therefore, the geometry is designed with the same scale as the experiment, so the nozzle exit diameter in the geometry has $D = 50.8$ mm. A 3-D view of the geometry domain is presented in Fig. 1a.

4.2 Mesh Configuration

The JAZzY code works with a geometry that is obtained from the rotation of a 2-D mesh that creates prismatic elements connecting the centerline. FLEXI code is restricted to hexahedral elements. Hence, in order to create two similar grids, the procedure of rotating a 2-D mesh was done differently. Instead of having a 2-D mesh starting in the centerline, it started with a diameter of $0.30D$ and the interior of the mesh is filled with a rectangular core connected to the rotated mesh. This strategy allows obtaining the same mesh topology for diameters larger than $0.30D$. A cut plane of the mesh used in the FLEXI simulations is presented in Fig. 1b.

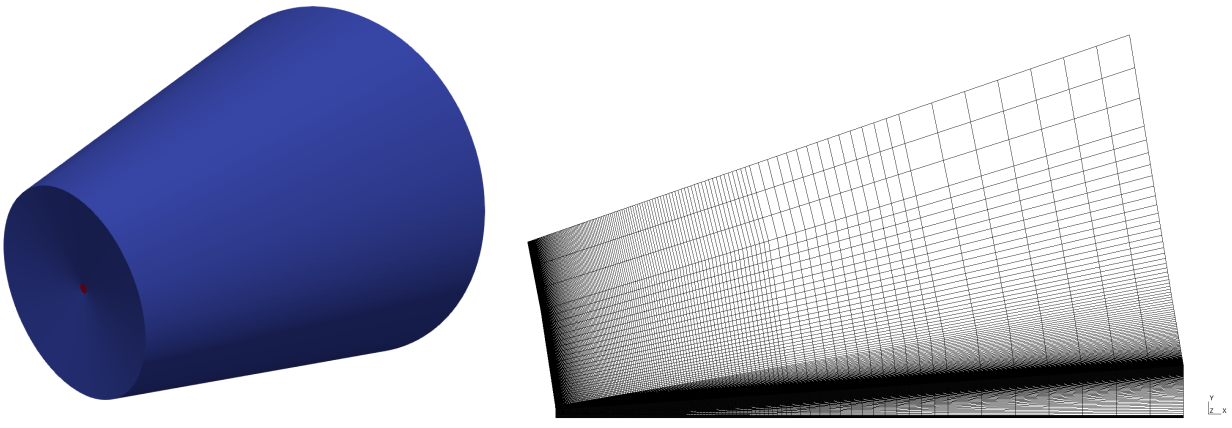

(a) (b)

Figure 1: (a): 3D view of geometry domain coloured by boundary condition. Red for jet inlet boundary condition and blue for the domain boundary condition. (b): Half cutplane of Flexi-2 mesh.

Due to the use of different numerical algorithms and orders of accuracy, it is necessary to establish comparison criteria for the simulations. For the JAZzY code, the number of degrees of freedom in each cell is one, because it only has one value of the properties in each cell. For the FLEXI code, the number of degrees of freedom in each cell depends on the

degree of chosen interpolating polynomial. For a second-order simulation, we have a first-order polynomial, that requires two internal nodes in each direction, and consequently, the degree of freedom in each element is 8. For a third-order simulation, 3 internal nodes are required in each simulation, leading to 27 degrees of freedom in each element.

Considering the degrees of freedom as the comparison criteria and the reference grid provided in Junqueira-Junior *et al.* (2018), with approximately 49×10^6 points, the two meshes created for the FLEXI code present approximately 6×10^6 and 2×10^6 elements. The adjustment of mesh sizes is obtained uniformly through the whole domain to guarantee consistency between the simulations. Table 1 presents a summary of the mesh refinements used in the current work. The present work uses GMSH (Geuzaine and Remacle, 2009) to generate the computational grids.

Table 1: Summary of the meshes utilized in the simulations.

Meshes	Order of Accuracy	DOF/cell	Cells (10^6)	Total # of DOF (10^6)
JAZzY	2nd order	1	49.1	49.1
Flexi-2	2nd order	8	6.2	49.6
Flexi-3	3rd order	27	1.8	48.6

4.3 Boundary Conditions

The present calculations apply the same boundary conditions of Junqueira-Junior *et al.* (2018) for the sake of consistency. For the jet inlet boundary condition, the red region in Fig. 1a, all properties are prescribed and a constant velocity is imposed. In the JAZzY simulation, the inflow boundary conditions imposed a non-dimensional jet velocity of 1.4, with non-dimensional pressure and temperature of 1.0, and a Reynolds number of 1.57×10^6. The inflow boundary condition of FLEXI simulations imposes a jet velocity of 476.37 m/s, with a pressure of $101,325$ Pa and a density of 1.225 kg/m^3, giving a Reynolds number based on the jet diameter of 1.66×10^6.

For the domain boundary condition, the blue region in Fig. 1a, Riemann invariant-type boundary conditions are used to characterize the farfield in the JAZzY code, while Dirichlet boundary conditions are used in FLEXI for the farfield boundary. A sponge zone (Flad *et al.*, 2014) is used in the simulations with FLEXI as an attempt to maintain the non-reflective properties of the Riemann invariants. This sponge region is implemented circumferentially, with a small damping value starting at approximately $14D$ and increased at longer distances from the centerline.

4.4 Calculation of Statistical Properties

For all the simulations, the initial condition is a stagnated flow all over the domain. Then, the jet is fully developed with approximated 3 flow-through times (FTT). One FTT is defined as the time taken by a particle with the jet velocity to cross the domain. For another 3 FTTs, the developed jet can reach the statistically steady condition. The statistics presented in this work are achieved from the following 3 FTTs. The complete simulation takes 9 FTTs. The JAZzY simulations run 14.2 FTTs before starting to collect statistical data for further 3.3 FTTs.

In the FLEXI simulations, the data are stored with a frequency of 100 kHz, which is at least 4 times larger than the acquisition frequency from the experiments. From the work of Junqueira-Junior *et al.* (2018), the data from the simulation using JAZzY are stored with a frequency of 280 kHz.

5. RESULTS

Two simulations are performed using the FLEXI code in the present work. The first calculation, Flexi S1, uses second-order accuracy and applies the Flexi-2 mesh, as described in Tab. 1. The second simulation, Flexi S2, runs with third-order spatial discretization and the Flexi-3 mesh, which has its properties also indicated in Tab. 1. The results of the simulations are compared with numerical (Junqueira-Junior *et al.*, 2018) and experimental data (Bridges and Wernet, 2008).

The simulations were performed using 3600 computational cores from the Jean-Zay supercomputer (IDRIS, 2021). The high scalability performance of the FLEXI code is discussed in the work of Hindenlang *et al.* (2012) and Krais *et al.* (2021). One interesting metric to compare the performance of the two numerical spatial discretization methods is the performance index (PID). The performance index is the time needed by the simulation to advance a single DOF one stage of the Runge-Kutta time integration scheme. It can be computed by

$$PID = \frac{wall\,clock\,time\;n_{cores}}{n_{DOF}\;n_{time\,steps}\;n_{RK-stages}}, \tag{12}$$

where $wall\,clock\,time$ is the time the simulation needed to perform $n_{time\,steps}$ time steps, n_{cores} is the quantity of cores used in the simulation, n_{DOF} is the number of DOF of the simulation and $n_{RK-stages}$ is the number of stages from the Runge-Kutta scheme. The simulation using the FLEXI code, running with 2nd-order accuracy in the Flexi-2

mesh, presented a PID of 7 μs/DOF. Similarly, the code running with the 3rd-order accurate option, using the Flexi-3 mesh, presented a PID of 13 μs/DOF. The JAZzY code also presents high scalability and detailed studies of the parallel performance of the code are presented in the work of Junqueira-Junior *et al.* (2019) and Junqueira-Junior *et al.* (2020).

The first results investigated are the distribution of mean longitudinal velocity component (<U>) and the distribution of root mean square (rms) of longitudinal velocity component fluctuation (u_{rms}) along the jet centerline ($y/D = 0$) and the jet lipline ($y/D = 0.5$). The velocity variables are non-dimensionalized by dividing by jet velocity U_j. The results are presented in Fig. 2. It is possible to observe from these results that velocity profiles calculated using the FLEXI numerical tool are very close to the one from JAZzY computation. Such a remark indicates little influence of the numerical method and order of accuracy for the conditions of such flow configuration.

The mean velocity distribution in the jet centerline, provided by the FLEXI simulations, Fig. 2a, presents a similar behavior of JAZzY calculations with a shorter potential core than the one observed in the experiments. After the velocity starts decreasing, the slope of the profile achieved by the simulations and the experimental measures is very similar. The shorter potential core may be correlated with the earlier increase in the velocity fluctuation, as presented in Fig. 2b, that all three numerical studies produced. In all simulations, it is possible to observe that the peaks in the calculated longitudinal velocity component fluctuations occur upstream of the one observed in the experimental data. Furthermore, such peaks in the computational results are considerably more pronounced than the ones observed in the experiments. The simulation with third-order of accuracy generates the smallest peaks among all calculations. However, it produces the largest double-peaked amplitude, which is a behavior reproduced by all numerical simulations that do not exist in the experiments.

The mean longitudinal velocity component distribution along the lipline, generated by all three calculations, Fig. 2c, once more show different results, presenting an earlier decrease in the velocity. Fig. 2d presents similar behavior for the rms values of velocity fluctuations in the lipline calculated using JAZzY and FLEXI, which present a sudden peak closer to the nozzle exit station that slowly decreases, while the experiment shows a slow increase of fluctuation velocity and the occurrence of the peak fluctuation farther from the nozzle exit station. The magnitude of the peak presented in the numerical simulations is significantly higher than the one presented in the experiments.

These results indicate an excessive turbulent intensity close to the nozzle outlet. Such a remark is possibly due to the choice of the inviscid top-hat velocity profile imposed at the inlet boundary condition. Other jet studies (Bogey and Bailly, 2010) indicate significant differences in the results due to the inflow condition. They run simulations changing the boundary layer thickness for initially laminar jets and notice that smaller boundary layer thickness generates sooner peaks of velocity fluctuation, which is probably the behavior observed in the simulations of this work.

Figure 3 presents the mean and the rms fluctuation of the longitudinal velocity profiles in four planes streamwise of nozzle flow at positions $x/D = 2.5$, $x/D = 5$, $x/D = 10$ and $x/D = 15$. Additional results of rms of transversal velocity fluctuation (v_{rms}) distribution and mean Reynolds shear-stress tensor component (<uv>) distribution are presented in the same figure. The results of transversal velocity fluctuation and Reynolds shear-stress tensor components are also non-dimensionalized by jet velocity.

The mean results of longitudinal velocity distribution are analyzed in the four planes, Figs. 3a-3d. In the first plane, Fig. 3a, the results indicate a good agreement between the simulations and experimental data, which indicates little influence of the inlet condition at the beginning of the jet. Downstream, in Fig. 3b, it is observed a larger spreading of velocity when comparing to the experimental reference, with peaks that are closer to the measured data when compared to the JAZzY profile. The results presented in the last two positions, Figs. 3c and 3d, show similar behavior, a large spreading of the velocity with a smaller peak than the one presented by experimental data.

Figures 3e to 3h illustrate results from rms of longitudinal velocity fluctuation. In the first position, Fig. 3e, it is observed the largest peak of fluctuation close to the lipline ($y/D = 0.5$) for all simulations. JAZzY simulation results indicate the highest peaks among all computational data. All calculations present values of u_{rms}/U_j very close to experimental at the centerline ($y/D = 0$). These results show that, very close to the nozzle exit, even with almost twice of velocity fluctuation, the mean velocity results are kept the same. The results of the second plane position, Fig. 3f, show that the largest velocity fluctuations produced at the lipline have already been transported to the centerline producing higher values of fluctuation than the ones observed in the experiments. Similar to what is observed in Fig. 3e, the results of JAZzY simulations still present higher levels of fluctuation than the ones obtained by FLEXI simulations. In the third plane, Fig. 3g, while the experimental data indicates that the fluctuation at the centerline has not yet achieved the levels of the lipline, in all the simulations the velocity fluctuation of the centerline presents similar values to the values observed at the lipline. The velocity fluctuations from the JAZzY simulation are still higher than the values obtained from FLEXI simulations, which are similar to the velocity fluctuation of the experiment. Figure 3h shows similar velocity fluctuations distributions transversally with the JAZzY simulations presenting the highest values.

The results from rms of transversal velocity fluctuation, presented in Figs. 3i to 3l, show similar distribution observed in the results from rms of longitudinal velocity distribution, Figs. 3e to 3h. The only difference is the fact that JAZzY and FLEXI results are ver similar for v_{rms}/U_j profiles.

The mean of the Reynolds shear-stress tensor component is illustrated in Figs. 3m to 3p. One can notice an important

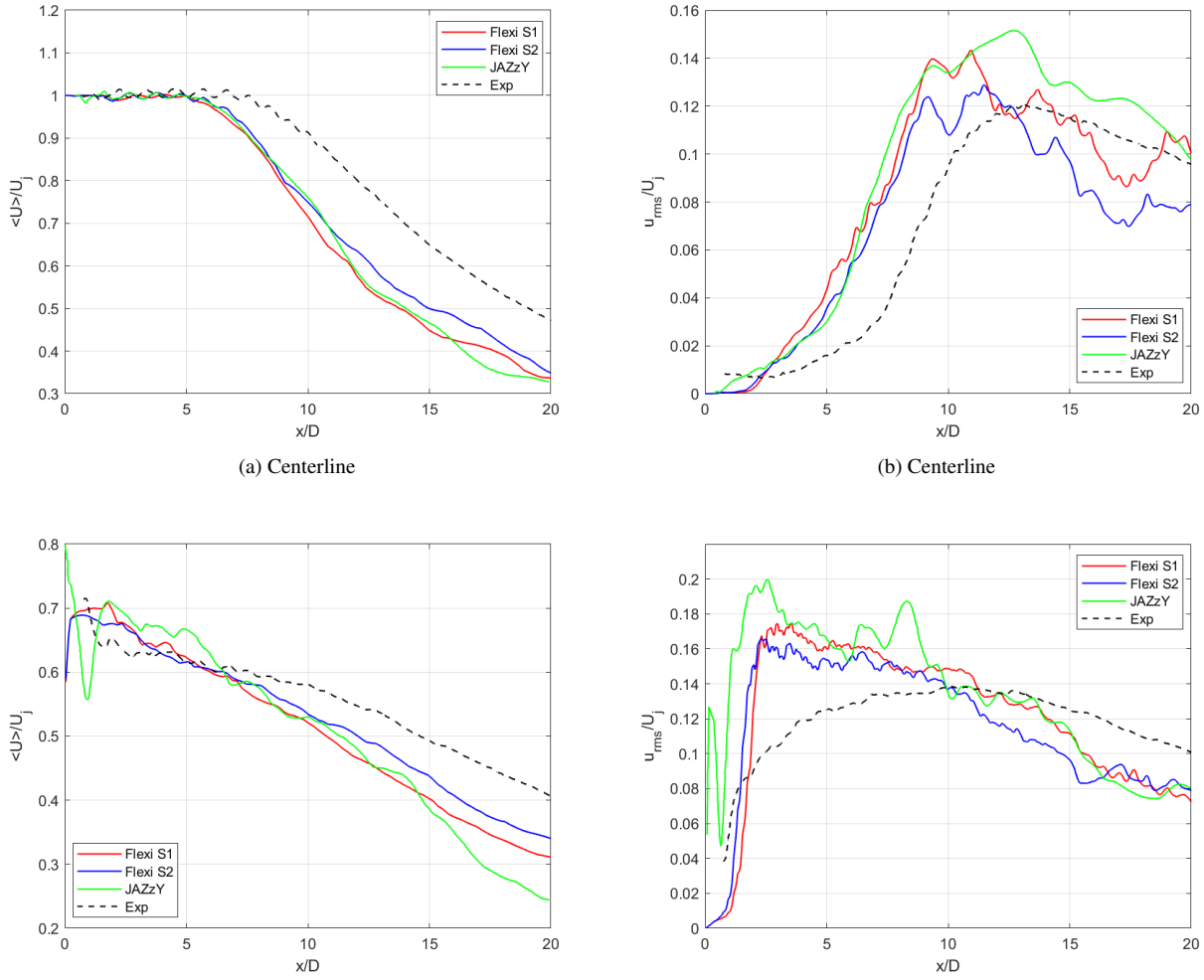

(a) Centerline

(b) Centerline

(c) Lipline

(d) Lipline

Figure 2: Results of mean longitudinal velocity component distribution (left) and rms of longitudinal velocity fluctuation (right) in the jet centerline $y/D = 0$ (top) and lipline $y/D = 0.5$ (bottom).

mismatch of JAZzY results when comparing the FLEXI and experimental profiles. Even in the first plane, Fig. 3m, the values of the Reynolds shear-stress tensor components obtained from the JAZzY simulation are much smaller than the results from FLEXI simulations. Moreover, the shape of the tensor distribution is also different presenting peaks with inverted signs while the FLEXI simulations produce one peak with the same direction of the experimental data. The advance to farther planes from the inlet jet show the decrease in the values of the Reynolds shear-stress tensor component for the results of FLEXI simulations, reaching values close to experimental data, while the results from JAZzY simulation show a reduction of one of the peeks and a movement of the peek to the centerline.

The mean velocity results show almost no difference between simulations performed in the present work and the reference calculations. The main differences are observed in the velocity fluctuations and the Reynolds shear-stress tensor component. The high levels of fluctuation produced in the JAZzY simulations may be related to the few artificial dissipation produced by the numerical method. The FLEXI simulations produced few levels of the fluctuations, which is similar to the levels produced in the experiment and the third order of accuracy simulation is the responsible for the few levels of velocity fluctuation. Even though, the third order accuracy is the most expensive simulation from all performed, it produced slightly better results for the same degree of freedom.

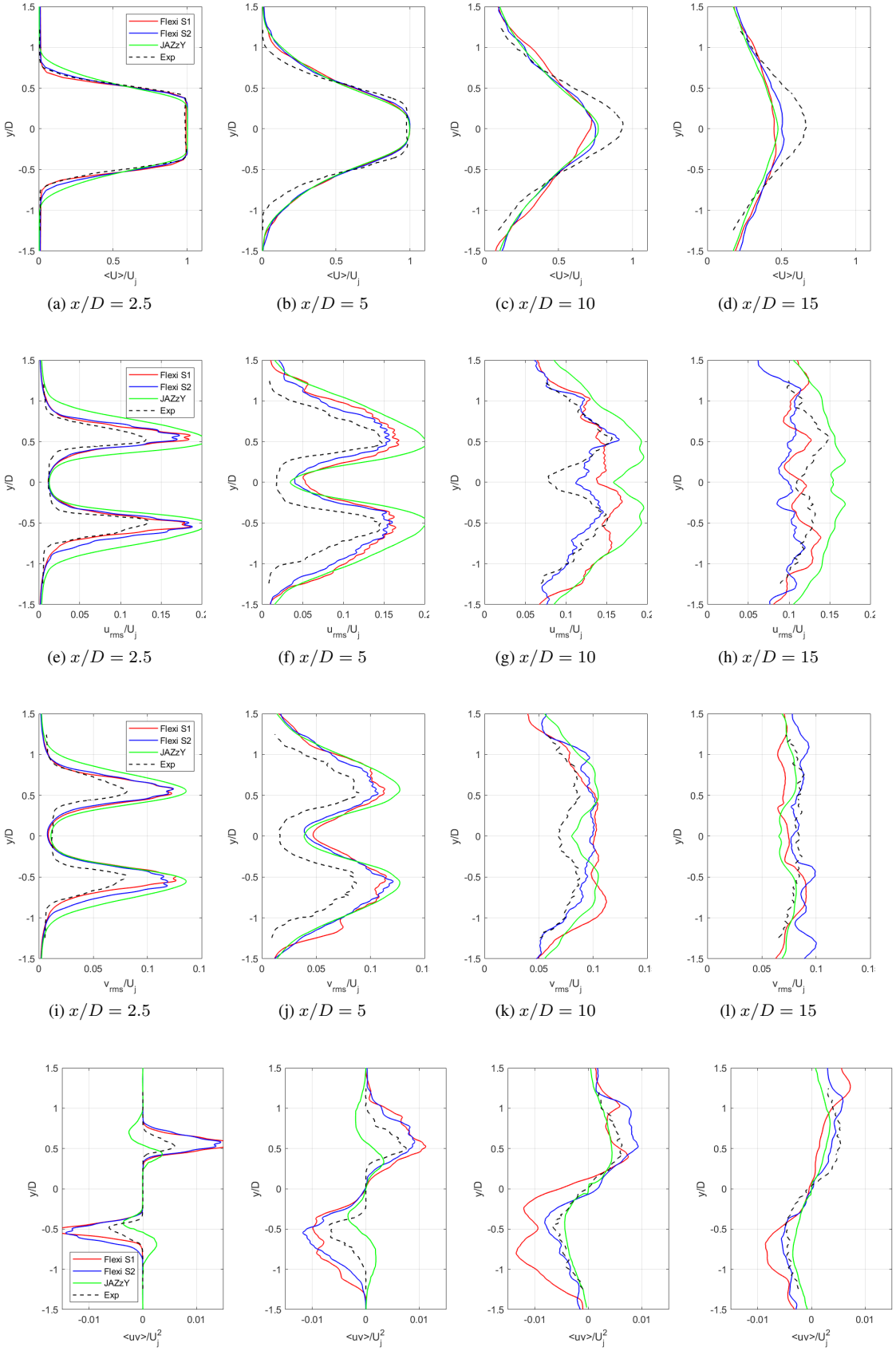

(a) $x/D = 2.5$ (b) $x/D = 5$ (c) $x/D = 10$ (d) $x/D = 15$

(e) $x/D = 2.5$ (f) $x/D = 5$ (g) $x/D = 10$ (h) $x/D = 15$

(i) $x/D = 2.5$ (j) $x/D = 5$ (k) $x/D = 10$ (l) $x/D = 15$

(m) $x/D = 2.5$ (n) $x/D = 5$ (o) $x/D = 10$ (p) $x/D = 15$

Figure 3: Results of mean longitudinal velocity component, rms of longitudinal velocity fluctuation, rms of transversal velocity fluctuation and mean Reynolds shear-stress tensor component (from top to bottom) are presented in four streamwise positions $x/D = 2.5$, $x/D = 5$, $x/D = 10$ and $x/D = 15$ (from left to right).

6. CONCLUSIONS

In this work, the authors investigated different numerical methods to simulate supersonic jet flows. The authors performed an analysis of previous calculations using JAZzY code, which uses finite difference method with second-order accuracy, and observed higher levels of velocity fluctuation in the lipline and the centerline, which caused a shorter potential core of the jet. Another framework, FLEXI, based on discontinuous Galerkin formulation on unstructured meshes, is used in this work to simulate the same problem with second-order accuracy and also third-order accuracy. The results obtained from FLEXI simulations are very similar to the results from JAZzY simulations.

The results of all simulations produced high peaks of velocity fluctuation close to the nozzle outlet. This high level of velocity fluctuation is transported to the jet centerline sooner than obtained in the experiments and consequently increased the levels of velocity fluctuation along the centerline. This phenomenon can be responsible for the short potential core of the jets obtained in the simulations. This result is also obtained in other works in the literature that investigated different velocity profiles imposed in the inflow condition for the jet.

Little influence is observed with different numerical methods for a fixed number of degree of freedom. The results of the simulation with third-order accuracy are the closest to experimental data, indicating that it is a strong candidate to be used for other configurations. Considering the results obtained, with almost no influence of different numerical methods and order of accuracy, the continuity of the work should be directed to the imposition of the nozzle exit boundary condition.

7. ACKNOWLEDGEMENTS

The authors acknowledge the support for the present research provided by Conselho Nacional de Desenvolvimento Científico e Tecnológico, CNPq, under the Research Grant No. 309985/2013-7. The work is also supported by the computational resources from the Center for Mathematical Sciences Applied to Industry, CeMEAI, funded by Fundação de Amparo à Pesquisa do Estado de São Paulo, FAPESP, under the Research Grant No. 2013/07375-0. The authors further acknowledge the National Laboratory for Scientific Computing (LNCC/MCTI, Brazil) for providing HPC resources of the SDumont supercomputer. This work was also granted access to the HPC resources of IDRIS under the allocation 2020-A0092A12067 made by GENCI. The first author acknowledges authorization by his employer, Embraer S.A., which has allowed his participation in the present research effort. The doctoral scholarship provide by FAPESP to the third author, under the Grant No. 2018/05524-1, is thankfully acknowledged. Additional support to the fourth author under the FAPESP Research Grant No. 2013/07375-0 is also gratefully acknowledged.

8. REFERENCES

Bassi, F. and Rebay, S., 1997. "A high-order accurate discontinuous finite element method for the numerical solution of the compressible Navier-Stokes equations". *Journal of Computational Physics*, Vol. 131, pp. 267–279.

Bogey, C. and Bailly, C., 2010. "Influence of nozzle-exit boundary-layer conditions on the flow and acoustic fields of initially laminar jets". *Journal of Fluid Mechanics*, Vol. 663, pp. 507–538.

Bridges, J. and Wernet, M.P., 2008. "Turbulence associated with broadband shock noise in hot jets". In *Proceedings of the 29th AIAA Aeroacoustics Conference,* AIAA Paper No. 2008-2834. Vancouver, British Columbia, Canada.

Carpenter, M.H. and Kennedy, C.A., 1994. "Fourt-order 2N-storage Runge-Kutta schemes". Technical Report NASA-TM-109112, NASA Langley Research Center.

Flad, D.G., Frank, H.M., Beck, A.D. and Munz, C.D., 2014. "A discontinuous Galerkin spectral element method for the direct numerical simulation of aeroacoustics". In *Proceedings of the 20th AIAA/CEAS Aeroacoustics Conference,* AIAA Paper No. 2014-2740. Atlanta, Georgia, United States.

Gassner, G.J. and Beck, A.D., 2013. "On the accuracy of high-order discretizations for underresolved turbulence simulations". *Theoretical and Computational Fluid Dynamics*, Vol. 27, pp. 221–237.

Gassner, G.J., Winters, A.R. and Kopriva, D.A., 2016. "Split form nodal discontinuous Galerkin schemes with summation-by-parts property for the compressible Euler equations". *Journal of Computational Physics*, Vol. 327, pp. 39–66.

Geuzaine, C. and Remacle, J.F., 2009. "GMSH: A three-dimensional finite element mesh generator with built-in pre- and post-processing facilities". *International Journal for Numerical Methods in Engineering*, Vol. 79, No. 11, pp. 1309–1331.

Harten, A. and Hyman, J.M., 1983. "Self adjusting grid methods for one dimensional hyperbolic conservation laws". *Journal of Computational Physics*, Vol. 50, pp. 253–269.

Hindenlang, F., Gassner, G.J., Altmann, C., Beck, A., Staudenmaier, M. and Munz, C.D., 2012. "Explicit discontinuous Galerkin methods for unsteady problems". *Computer & Fluids*, Vol. 61, pp. 86–93.

IDRIS, 2021. "IDRIS - Jean Zay: HPE SGI 8600 supercomputer". IDRIS, Institute for Development and Resource in Intensive Scientific Computing, http://www.idris.fr/eng/jean-zay/cpu/jean-zay-cpu-hw-eng.html. Accessed 12 August 2021.

Jameson, A. and Mavriplis, D., 1986. "Finite volume solution of the two-dimensional Euler equations on a regular triangular mesh". *AIAA Journal*, Vol. 24, No. 4, pp. 611–618.

Junqueira-Junior, C., Azevedo, J.L.F., Panetta, J., Wolf, W.R. and Yamouni, S., 2019. "Strong scaling of numerical solver for supersonic jet flow configurations". *Journal of the Brazilian Society of Mechanical Sciences and Engineering*, Vol. 41, No. 547.

Junqueira-Junior, C., Azevedo, J.L.F., Panetta, J., Wolf, W.R. and Yamouni, S., 2020. "On the scalability of CFD tool for supersonic jet flow configurations". *Parallel Computing*, Vol. 93, p. 102620.

Junqueira-Junior, C., Yamouni, S., Azevedo, J.L.F. and Wolf, W.R., 2018. "Influence of different subgrid-scale models in low-order LES of supersonic jet flows". *Journal of the Brazilian Society of Mechanical Sciences and Engineering*, Vol. 40, No. 258, pp. 1–29.

Kopriva, D.A. and Gassner, G., 2010. "On the quadrature and weak form choices in collocation type discontinuous Galerkin spectral element methods". *Journal of Scientific Computing*, Vol. 44, pp. 136–155.

Krais, N., Beck, A., Bolemann, T., Frank, H., Flad, D., Gassner, G., Hindenlang, F., Hoffmann, M., Kuhn, T., Sonntag, M. and Munz, C.D., 2021. "FLEXI: A high order discontinuous Galerkin framework for hyperbolic–parabolic conservation laws". *Computers and Mathematics with Applications*, Vol. 81, pp. 186–219.

Pirozzoli, S., 2011. "Numerical methods for high-speed flows". *Annual Review of Fluid Mechanics*, Vol. 43, pp. 163–194.

Smagorinsky, J., 1964. "General circulation experiments with the primitive equations: I. The basic experiment". *Monthly Weather Review*, Vol. 93, No. 3, pp. 99–164.

Sonntag, M. and Munz, C.D., 2017. "Efficient parallelization of a shock capturing for discontinuous Galerkin methods using finite volume sub-cells". *Journal of Scientific Computing*, Vol. 70, pp. 1262–1289.

Turkel, E. and Vatsa, V.N., 1994. "Effect of artificial viscosity on three-dimensional flow solutions". *AIAA Journal*, Vol. 32, No. 1, pp. 39–45.

Vreman, A.W., 1995. *Direct and Large Eddy Simulation of the Compressible Turbulent Mixing Layer*. Ph.D. thesis, University of Twente, Twente, Netherlands.

9. RESPONSIBILITY NOTICE

The authors are solely responsible for the printed material included in this paper.